https://doi.org/10.1007/s41230-024-4036-3

New poly-types of LPSO structures in a non-equilibrium $Mg_{97}Zn_1Y_{1.6}Ca_{0.4}$ alloy

**Qian-qian Jin[1, 2], Zi-hui Tang[1], Wen-long Xiao[2], Xiu-yu Qu[2], **Xu-hao Han[2], Lin Mei[2], Xiao-hong Shao[3], and Xiu-liang Ma[4]

1. School of Biological and Chemical Engineering, Guangxi University of Science and Technology, Liuzhou 545006, Guangxi, China

2. Center for the Structure of Advanced Matter, School of Electronic Engineering, Guangxi University of Science and Technology, Liuzhou 545006, China

3. Shenyang National Laboratory for Materials Science, Institute of Metal Research, Chinese Academy of Sciences, Shenyang 110016, China

4. Bay Area Center for Electron Microscopy, Songshan Lake Materials Laboratory, Dongguan 523808, Guangdong, China

Abstract: In this study, a comprehensive analysis of microstructural features, morphology, crystal structures, and interface structures of long-period stacking ordered (LPSO) structures in a non-equilibrium $Mg_{97}Zn_1Y_{1.6}Ca_{0.4}$ alloy cast in a steel mold was carried out. The addition of Ca element plays an important role in the refinement of LPSO structure. The result reveals new poly-types including 20H F2F2F4, 60R $(F2F3\overline{F}3)_3$, and 66H F2F3$\overline{F}$ $3F2(F6)_4$ featuring a 6-Mg structure, alongside the prevalent 18R and 14H LPSO structures. The incoherent interface between 20H and the Mg matrix is split into two dislocation arrays, leading to the formation of a segment of $60R_1$. Moreover, the superstructure 116L, designated as $(F2)_{18}F4$, is formed through the ordered distribution of F4 stacking faults in 18R.

Keywords: LPSO structures; crystal structure; Mg alloys; heterogeneous interface

CLC numbers: TG146.22 **Document code:** A

1 Introduction

Conventional magnesium alloys often encounter challenges such as poor corrosion resistance, thermal stability, and inferior mechanical properties at high temperatures [1, 2]. To address these limitations, various strategies have been employed, including chemical composition modification [3, 4], homogenization [5, 6], precipitation hardening [7, 8], texture modification [9-11], and grain refinement [12]. Recently, numerous investigations have been conducted focusing on Mg-M-RE alloys (where M comprises Al, Co, Ni, Cu, Zn, and Ga; and RE includes Y, Gd, Tb, Dy, Ho, Er, and Tm) due to their exceptional mechanical properties [13-15] and unique structural features [16, 17]. For instance, the $Mg_{97}Zn_1Y_2$ alloy, synthesized through rapid solidification powder metallurgy, demonstrated an impressive tensile yield strength exceeding 600 MPa at room temperature and an elongation of about 5% [13, 14]. Subsequent Mg-M-RE alloys have exhibited tensile yield strengths ranging from 297 to 377 MPa [18-20]. The outstanding mechanical properties of Mg-M-RE alloys primarily originate from both grain refinement and the presence of long-period stacking ordered (LPSO) structures [13-15]. The formation of LPSO structures involves the periodic introduction of AB′C′A blocks into the hexagonal close-packed structure, with the prime-annotated letters indicating layers enriched with M/RE elements [21, 22]. These LPSO structures can exhibit both hexagonal (H) and rhombohedral (R) Bravais lattices, depending on their stacking sequence.

To comprehend the varied configurations of LPSO structures, explore their formation mechanisms, and establish inherent connections with the mechanical properties of magnesium alloys, extensive analytical studies have been undertaken, emphasizing their microstructure [23-30]. In this regard, various LPSO structures have been identified in different magnesium alloys [31-34]. In Mg-Zn-Y alloys, configurations such as 10H, 18R, 14H, and 24R have been observed, wherein 1, 2, 3, and 4 layers of magnesium atoms interspersed

*Qian-qian Jin

Ph. D., Associate Researcher. His research interests mainly focus on the transmission electron microscopy of new crystal structures and interface defects in magnesium alloys.

E-mail: qqjin10s@139.com

**Xu-hao Han

E-mail: 491266846@qq.com

Received: 2024-02-23; Accepted: 2024-06-18

between every two neighboring AB′C′A blocks [18-22, 29, 35]. In Mg-Co-Y alloys, structures such as 15R, 12H, and 21R have been identified, featuring 2, 3, and 4 layers of magnesium atoms between every two neighboring AB′C blocks [32]. Moreover, Jin et al. [33, 34] discovered six additional LPSO structures, including 72R, 29H, 102R, 192R, 51R, and 60H, in a $Mg_{92}Co_2Y_6$ alloy. These structures incorporate both AB′C′A and AB′C blocks [33]. Furthermore, an ultra-long 654R structure, derived from an ordered arrangement of 15R and 12H components, has been identified in a $Mg_{88}Co_5Y_7$ alloy [34].

In $Mg_{97}Zn_1Y_2$ alloys, the diameters of Mg, Zn, and Y atoms adhere to the sequence r_{Zn}(0.133 nm)<r_{Mg}(0.16 nm)<r_Y(0.18 nm). This specific arrangement of their atomic diameters facilitates the formation of Zn_6Y_8 or Zn_6Y_8(Mg, Zn, Y) clusters, effectively minimizing compression and extension strains associated with Y and Zn atoms, respectively [33]. It is significant that calcium (Ca), with a larger atomic diameter of 0.197 nm compared to the Mg atom, emerges as a promising candidate for the stable formation of the LPSO phase [36]. Furthermore, the addition of Ca enhances the mechanical properties of Mg alloys with LPSO structures [37] and improves corrosion resistance [38]. Therefore, it is imperative to explore the potential substitution of Y atoms with Ca in LPSO structures and assess the influence of Ca addition on the morphology and crystal structure of LPSO formations. This exploration aims to reduce the cost of $Mg_{97}Zn_1Y_2$ alloys and enhance their mechanical properties.

In this study, a non-equilibrium solidified $Mg_{97}Zn_1Y_{1.6}Ca_{0.4}$ alloy was fabricated by casting in a steel mold with a rapid cooling rate. Microscopic morphology was observed using spherical aberration-corrected transmission electron microscopy, and the composition was analyzed through energy dispersive spectroscopy (EDS). This analysis aimed to analyze the microstructural characteristics of non-equilibrium solidified magnesium alloys, with a focus on elucidating the formation mechanism of LPSO structures.

2 Experimental section

A quaternary alloy with a composition of $Mg_{97}Zn_1Y_{1.6}Ca_{0.4}$ was prepared by melting high-purity Mg, Zn, Mg-30wt.% Y, and Mg-30wt.% Ca master ingots in a resistance furnace under a protective mixed gas of SF_6 (0.5vol.%) and CO_2 (99.5vol.%), followed by casting in a steel mold preheated to 400 °C. The cavity size of the mold was 40 mm in width, 150 mm in length, and 20 mm in thickness. Micromorphology was observed using scanning electron microscopy (SEM; JEOL JEM-6390LA). Thin-foil samples for TEM and STEM observations were prepared through cutting, mechanical grinding, dimpling, and Ar ion milling while employing the Gatan Precision Ion Polishing System (PIPS 695). An aberration-corrected scanning transmission electron microscope (JEM ARM 200F, Japan) with a cold field emission gun operated at 200 kV was employed for microstructure and composition analysis. X-ray energy dispersive spectroscopy (EDS) was performed using a detector (JEOL JED2300, Country). The probe convergence angle and collection semi-angle were 20.6 mrad and 54–220 mrad, respectively. All HAADF-STEM images were captured along $[2\bar{1}\bar{1}0]_\alpha$ axis. Novel methodologies have been introduced for the analysis of the stacking sequence in LPSO structures and for determining their corresponding Bravais lattices and space groups in Mg-M-RE alloys [33]. AB′C′A (and/or AC′B′A) blocks are defined as F-blocks and denoted as F (and/or $\bar{F}$). The Mg layers sandwiched between the F-blocks are written as *n*-Mg. The subscript reflects the number of repeated (sub) unit cells.

3 Results

3.1 SEM observation of LPSO structures

Figure 1 illustrates a back-scattered electron (BSE)-SEM image of the as-cast $Mg_{97}Zn_1Y_{1.6}Ca_{0.4}$ alloy, where the contrast correlated with the chemical composition. In BSE-SEM conditions, the Mg matrix appears dark, reflecting the average (standard deviation) for the atomic percentage of the Mg matrix composition: Mg: 99.39 (0.16), Zn: 0.34 (0.17), Y: 0.16 (0.04), Ca: 0.11 (0.07). The bulk LPSO structure is characterized by a light contrast, reflecting the average (standard deviation) for its atomic composition: Mg: 89.43 (0.88), Zn: 5.61 (0.51), Y: 4.48 (0.30), Ca: 0.48 (0.07). Moreover, an intergrowth structure of LPSO and Mg matrix, displaying grey contrast, is observed. This contrast is induced by the refinement effect of the Ca element [38, 39]. Unidentified phases in white contrast are denoted by yellow arrows, where the Ca element is in the minority.

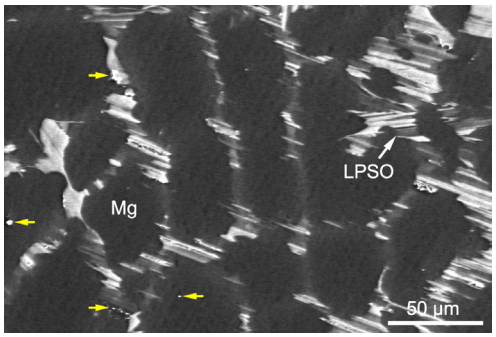

Fig. 1: A BSE-SEM micrograph showing an overview of as-cast $Mg_{97}Zn_1Y_{1.6}Ca_{0.4}$ alloy

3.2 New poly-types of LPSO structures

Figure 2 depicts Z-contrast images recorded from the Mg matrix in the as-cast $Mg_{97}Zn_1Y_{1.6}Ca_{0.4}$ alloy along the $[2\bar{1}\bar{1}0]$ zone axis. The bulk LPSO structure displays a bright contrast caused by the enrichment of Zn and Y atoms, while the Mg matrix reveals a dark contrast. The bright and dark stripes reflect the intergrowth of thin LPSO structures and the Mg matrix. Figure 2(b) reveals the 14H and 18R LPSO structures in bright contrast, along with large planar defects in the Mg matrix indicated by the long bright lines. Moreover, Fig. 2(c) illustrates large planar defects and LPSO structures containing 1 to 6 blocks, with the volume fraction of the LPSO structures

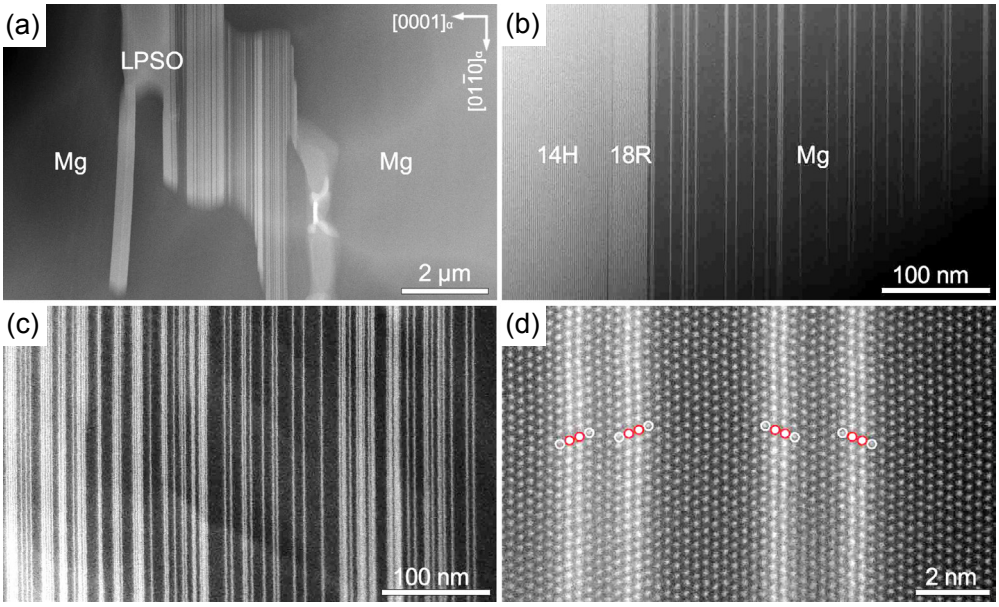

Fig. 2: Distribution of LPSO structures in Mg matrix (a), intergrowth of 14H, 18R and Mg matrix containing planar defects (b), distribution of ultrafine LPSO structures in Mg matrix (c), and stacking sequence of ultrafine LPSO structures in Mg matrix (d)

reaching up to 1/3. The high-resolution Z-contrast image depicted in Fig. 2(d) demonstrates that all the planar defects and LPSO structures consist of AB′C′A blocks.

Figure 3 illustrates Z-contrast images of LPSO structures obtained from a $Mg_{97}Zn_1Y_{1.6}Ca_{0.4}$ alloy. In the low-magnification HAADF-STEM image illustrated in Fig. 3(a), AB′C′A blocks exhibiting bright contrast are separated by *n*-Mg structure exhibiting dark contrast in Regions a and c, forming stacking disordered structures. In Region b, three AB′C′A blocks, sandwiched by four thick *n*-Mg structures, and five AB′C′A blocks, separated by thin *n*-Mg structures, are arranged alternatively. The incoherent interface between the LPSO structures and Mg is not parallel to the $(01\bar{1}0)$ plane. Figure 3(b) shows the corresponding atomic-resolution HAADF-STEM image in Region b. Two repeated unit cells $F2F3\bar{F}3F2(F6)_2F8F4$ and five repeated unit cells $F2F3\bar{F}3F2(F6)_4$ are observed. The correlation between the first layer of a closely packed structure and the next layer follows either $\boldsymbol{s}_1=\boldsymbol{e}$, $\boldsymbol{s}_2=\frac{2}{3}\boldsymbol{a}+\frac{1}{3}\boldsymbol{b}+\boldsymbol{e}$, or $\boldsymbol{s}_3=\frac{1}{3}\boldsymbol{a}+\frac{2}{3}\boldsymbol{b}+\boldsymbol{e}$, where $\boldsymbol{a}$ and $\boldsymbol{b}$ denote hexagonal basic translational vectors in the layer, and $\boldsymbol{e}$ is a vector perpendicular to $\boldsymbol{a}$ and $\boldsymbol{b}$. The translation of the F(2*k*) structure is $\boldsymbol{s}_3$, and the translation of the F(2*k*+1) and $\bar{\text{F}}(2k+1)$ structure is $\boldsymbol{s}_1$ [40]. It should be indicated that both $F2F3\bar{F}3F2(F6)_2F8F4$ and $F2F3\bar{F}3F2(F6)_4$ structures contain 66 layers. The $F2F3\bar{F}3F2(F6)_4$ structure is dominant and its translation can be calculated to be $\boldsymbol{s}_1$. Consequently, the $F2F3\bar{F}3F2(F6)_4$ structure can be denoted as 66H. Inversion center $\bar{1}$ exists at the center of F and $\bar{\mathbf{F}}$ blocks in bold in the $F2F3\bar{\mathbf{F}}3F2F6F6\mathbf{F}6F6$ structure, and its space group is $P\bar{3}m1$. For $a_{66H}=a_{Mg}$ and $c_{66H}=\frac{1}{2}\times66\times c_{Mg}$, lattice parameters in hexagonal coordinate are a=0.321 nm and c=17.2 nm.

Figure 4(a) displays a low-magnification HAADF-STEM micrograph of the step-like LPSO/Mg interfaces,

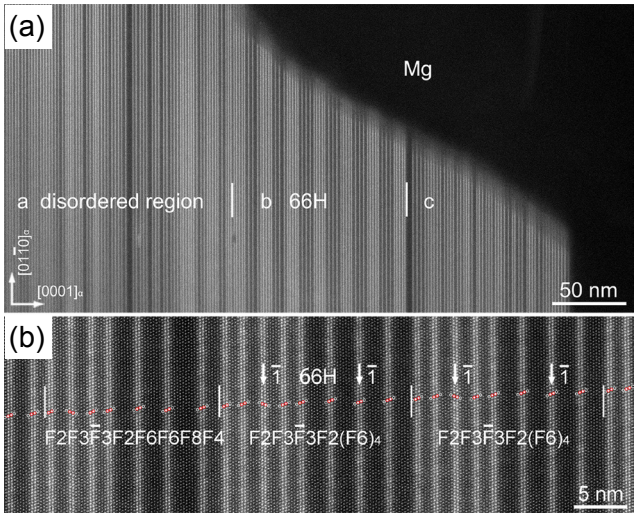

Fig. 3: HAADF-STEM image of LPSO structures obtained from a $Mg_{97}Zn_1Y_{1.6}Ca_{0.4}$ (at.%) alloy along the $[2\bar{1}\bar{1}0]$ zone axis of the Mg matrix: (a) low-magnification HAADF-STEM image showing stacking ordered structures 66H and stacking disordered structures; (b) atomic-resolution HAADF-STEM image shows the structure details of 66H in Region b

encompassing (0001) coherent boundaries and $(01\bar{1}0)$ semi-coherent boundaries. The right part of the LPSO structure is identified as 18R containing F4 stacking faults, as illustrated by atomic-scale HAADF-STEM images [41]. Figure 4(b) reveals a new structure on the left part with a stacking sequence of F2F2F4. The translation of F2F2F4 is calculated to be $\boldsymbol{s}_1$. Accordingly, the structure is determined to be a hexagonal Bravais lattice comprising 20 layers, denoted as 20H. Inversion centers are observed at the central positions of 4-Mg and F-block structures, as indicated by white arrows. Therefore, the space group of this structure is determined to be $P\bar{3}m1$. For $a_{20H}=a_{Mg}$ and $c_{20H}=\frac{1}{2}\times20\times c_{Mg}$, its lattice parameters in hexagonal coordinate are a=0.321 nm and c=5.21 nm.

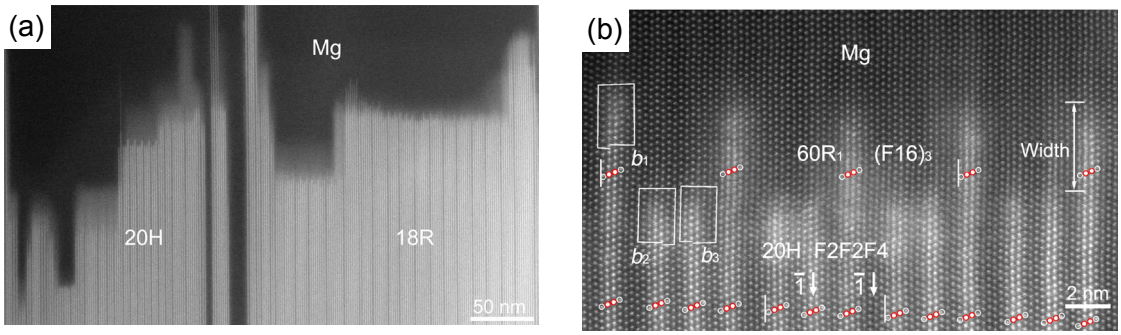

Fig. 4: Low-magnification HAADF-STEM image showing the semi-coherent (SC) interface between Mg and LPSO structures (a), atomic-resolution HAADF-STEM image of crystal structure of 20H and interface structure between 20H and Mg matrix (b). Pure edge dislocations b_1, and mixed dislocations b_2 and b_3 are arranged periodically, recorded along the $[2\bar{1}\bar{1}0]_\alpha$ axis.

A distinct structure, characterized by a repeating unit F16, is identified at the interface between 20H and the matrix. This novel structure is designated as 60R$_1$, and its stacking sequence is represented as (F16)$_3$, corresponding to the translations of F16 being $\boldsymbol{s}_2$ [33]. Arrays of $\boldsymbol{b}_1$ dislocations, along with arrays of $\boldsymbol{b}_2$ and $\boldsymbol{b}_3$ dislocations, are observed arranged on $(01\bar{1}0)$ planes in a repetitive pattern, as indicated in Fig. 4(b). The 60R$_1$/Mg interface comprises purely edge (90°) Shockley partial dislocations, where the Burgers vector $\boldsymbol{b}_1$ is defined as $1/3[0\bar{1}10]$. In contrast, the 18R/60R$_1$ interface involves a combination of $\boldsymbol{b}_2$ and $\boldsymbol{b}_3$ mixed (30°) Shockley partial dislocations. Consequently, it can be inferred that $\boldsymbol{b}_2=1/3[10\bar{1}0]$ and $\boldsymbol{b}_3=1/3[\bar{1}100]$ (or $\boldsymbol{b}_2=1/3[\bar{1}100]$ and $\boldsymbol{b}_3=1/3[10\bar{1}0]$), with their screw components having the same magnitude but showing opposite signs. Moreover, there is a slight tilt angle of 2.03°, observed between $(0001)_{60R1}$ and $(0001)_{Mg}$ or between $(0001)_{60R}$ and $(0001)_{18R}$, caused by two dislocation arrays in the 60R$_1$/Mg and 60R$_1$/18R interfaces, respectively. The width of 60R$_1$ is measured at about 3.4 nm ($2.2y_0$), exceeding the thermodynamic equilibrium width of ($1.8y_0$) [42, 43]. The interaction between solute atoms and dislocation is proportional to the edge component of its Burgers vector. The stronger interaction between solute atoms and $\boldsymbol{b}_1$ dislocations can be anticipated, given $b_{1e}=2b_{2e}=2b_{3e}$, facilitating the motion of $\boldsymbol{b}_1$ dislocations compared to the double-core dislocations $\boldsymbol{b}_2$ and $\boldsymbol{b}_3$. Therefore, the observed phenomenon elucidates the reason behind the width of 60R$_1$ surpassing the thermodynamic equilibrium width.

Figure 5(a) depicts a high-resolution HAADF-STEM image of a complex LPSO structure within a $Mg_{97}Zn_1Y_{1.6}Ca_{0.4}$ alloy obtained along the $[2\bar{1}\bar{1}0]_\alpha$ axis. The recurring structure denoted as F2F3$\bar{\text{F}}$3, comprises 20 layers. The translations of LPSO structure's components were introduced [40]. The relation between the first layer of a structure and the layer following the structure is one of the three translations, $\boldsymbol{s}_1=\boldsymbol{e}$, $\boldsymbol{s}_2=\frac{2}{3}\boldsymbol{a}+\frac{1}{3}\boldsymbol{b}+\boldsymbol{e}$ and $\boldsymbol{s}_3=\frac{1}{3}\boldsymbol{a}+\frac{2}{3}\boldsymbol{b}+\boldsymbol{e}$, where $\boldsymbol{a}$ and $\boldsymbol{b}$ denote hexagonal basic translational vectors within the layer, and $\boldsymbol{e}$ is a vector perpendicular to $\boldsymbol{a}$ and $\boldsymbol{b}$. The translation of F2 is $\boldsymbol{s}_3$, The translation of F3 or $\bar{\text{F}}$3 is $\boldsymbol{s}_1$, and the translation of

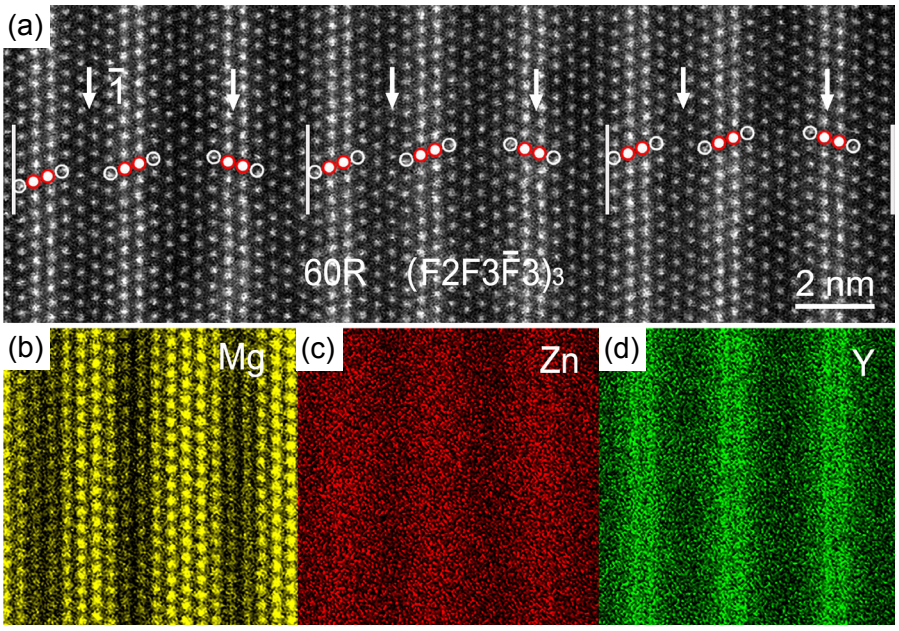

Fig. 5: Atomic-resolution HAADF image of 60R (a), corresponding EDS mappings (b–d) of the 60R structure showing the distribution of Mg (b), Zn (c), and Y (d), recorded along the $[2\bar{1}\bar{1}0]_\alpha$ axis

a repeated unit is the sum of all the structure components' translations. The translation of F2F3$\bar{3}$F3 can be calculated as $\boldsymbol{s}_3+\boldsymbol{s}_1+\boldsymbol{s}_1=\boldsymbol{s}_3$. Thus, it is identified as a 60R structure and expressed as (F2F3$\bar{3}$F3)$_3$. The space group is defined as $R\bar{3}m$, with inversion centers located at the center of 2-Mg and F-block structures, as indicated by arrows in Fig. 5(a). For $a_{60R}=a_{Mg}$ and $c_{60R}=\frac{1}{2}\times 60\times c_{Mg}$, the lattice parameters in hexagonal coordinate are a=0.321 nm and c=15.6 nm.

The chemical composition of the 60R LPSO structure is identified as $Mg_{82.22}Zn_{7.28}Y_{10.44}Ca_{0.05}$. This analysis confirms that Ca atoms cannot substitute for Y atoms within the LPSO structure. Atomic EDS mappings, illustrating the distributions of Mg, Zn, and Y atoms, are presented in Figs. 5(b–d), respectively. A brighter contrast in Fig. 5(b) corresponds to the 2-Mg and 3-Mg structures, while in Figs. 5(c–d), the B′ and C′ layers within the AB′C′A blocks exhibit bright contrast. These EDS maps support the conclusion that Zn/Y elements are enriched in the AB′C′A blocks of the 60R structure, primarily in the layers denoted by primes, consistent with the observations in $Mg_{97}Zn_1Y_2$ alloys [40].

3.3 Stacking faults (SFs) in 18R LPSO structures

SFs within the 18R structure typically reveal disorder, as illustrated in Fig. 4(a). However, Fig. 6(a) reveals that ordered or statistically ordered SFs can be occasionally observed within the 18R. The detailed structure is analyzed through atomic-resolution HAADF-STEM images in Figs. 6(b–c). The most common and less common stacking faults are F4 and F3$\bar{3}$F3, respectively, denoted by white arrows. The structure in Fig. 6(a) can be described by the (F2)$_p$F4 and (F2)$_p$F3$\bar{3}$F3 structures. The number p was counted and tabulated in Fig. 6(a). As the superstructure is induced by SFs and the stacking sequence is not strictly repetitive, its Bravais lattice and space group are not discussed here. The dominant structures are (F2)$_{18}$F4 and (F2)$_{16}$F4, with an average number of p around 18. Therefore, this superstructure is denoted as (F2)$_{18}$F4 and named 116L, signifying that the superstructure comprises 116 layers.

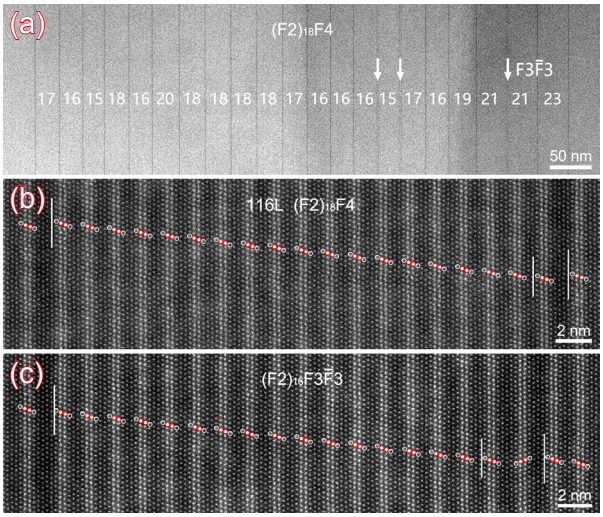

Fig. 6: HAADF-STEM image of superstructure 116L (a), atomic-resolution HAADF-STEM images of 18R containing F4 (b) and F3$\bar{3}$F3 (c) SFs

4 Discussion

The microstructural characteristics of LPSO structures in the $Mg_{97}Zn_1Y_{1.6}Ca_{0.4}$ alloy were thoroughly investigated, encompassing morphology, distribution, crystal structures, and interface structures various aspects. Significantly, the LPSO structures in this alloy are considerably thinner compared to those observed in the near-equilibrium $Mg_{97}Zn_1Y_2$ alloy [42]. This thinning trend is consistent with experimental results in the $Mg_{97}Zn_1Y_2$-$x$wt.%Ca alloys [38]. Particularly, the absence of $Ca_2Mg_6Zn_3$ in samples may originate from the lower concentration of Ca atoms in the alloy.

In this alloy, the predominant LPSO structures reveal 18R and 14H characteristics. However, the unexpected presence of n-Mg structures introduced a myriad of novel polytypes of LPSO structures and stacking-disordered configurations, as illustrated in Fig. 3. Previously documented LPSO structures in Mg-M-RE (M=Zn, Cu, Ni, Al; RE=rare earth) alloys, including 12R, 10H, 18R, 14H, 24R, feature AB′C′A blocks, with 0 to 4 Mg layers sandwiched in between [19, 21, 30, 44]. The analysis in a near-equilibrium $Mg_{97}Zn_1Y_2$ alloy reveals eight additional polytypes of LPSO structures, encompassing 60R, 78R, 26H, 96R, 38H, 40H, 108H, and 246R, each containing AB′C′A blocks along with 2-Mg and 3-Mg structures [40]. In the current alloy, a complex 66H structure featuring a 6-Mg structure, along with 60R, 60R$_1$, and 20H structures, was observed only once. However, it is significant that the introduced trace amount of Ca does not replace the Y atoms in LPSO structures, as depicted in Fig. 5. Table 1 provides expressions and crystallographic parameters of these newly identified LPSO structures in Mg-M-RE-based alloys. Moreover, the coexistence of LPSO structure laths and Mg laths is commonly observed, accompanied by high-density planar defects and LPSO structures containing 1–6 AB'C'A blocks distributed within the Mg matrix. The volume fraction of LPSO structures may reach up to one-third of Mg matrix, all featuring AB'C'A blocks. Occasional stacking faults are observed in 18R, and their ordered distribution leads to the formation of superstructures, exemplified by 116L, which exhibited similar structrure character with 62L in previous work [41]. The disordered distribution of stacking faults in 18R disrupted the periodicity of the 18R/Mg interface. These findings suggest that the presence of Ca atoms further reduces the stacking fault energy in Mg alloys, promoting a more homogeneous intergranular LPSO structure. Considering that the introduction of Ca to Mg alloys with LPSO structures enhances corrosion resistance [38], the relatively thin LPSO structures and/or AB'C'A blocks induced by trace Ca addition, as depicted in Fig. 2, may be an effective parameter.

Similar to the occurrence of 54R at the 18R/Mg interface in both near-equilibrium and non-equilibrium Mg-Zn-Y alloy [42, 43], the presence of 60R$_1$ is observed at the 20H/Mg interface. The Bravais lattice type of 20H and 18R LPSO structures is hexagonal and rhombohedral, respectively. However, their stacking sequences, F2F2F4 and F2F2F2, respectively, reveal similarities. No tilt or twist misorientation between 20H (or

Table 1: Parameters of new LPSO structures in Mg-M-RE-based alloys

LPSO	Expressions	c (nm)	Space groups	
60R	$(F2F3\bar{F}3)_3$	15.6	$R\bar{3}m$	The present study
66H	$F2F3\bar{F}3F2(F6)_4$	17.2	$P\bar{3}m$	The present study
66H	$F2F3\bar{F}3F2(F6)_2F8F4$	17.2	$P3m$	The present study
20H	F2F2F4	5.21	$P\bar{3}m1$	The present study
$60R_1$	$(F16)_3$	15.6	$R\bar{3}m$	The present study
54R	$(F14)_3$	14.1	$R\bar{3}m$	[43]
54R1	$(F2F8)_3$	14.1	$R\bar{3}m$	[42, 43]
116L	$(F2)_{18}F4$	25.0	–	The present study

18R) and Mg matrix is detected, which indicates that the sum of both edge components and screw components of three interfacial dislocations in a unit cell is zero. $\boldsymbol{b}_1=1/3[0\bar{1}10]$, $\boldsymbol{b}_2=1/3[10\bar{1}0]$, and $\boldsymbol{b}_3=1/3[\bar{1}100]$. Hence, the strong interaction force between two neighboring $\boldsymbol{b}_2$ and $\boldsymbol{b}_3$ dislocations with opposite screw components would always be attractive. The pure edge dislocation array $\boldsymbol{b}_1$ and double-core dislocation array $\boldsymbol{b}_2/\boldsymbol{b}_3$ are most stable while lying on the $(01\bar{1}0)$ planes, which are dominated by the elastic interaction between neighbor $\boldsymbol{b}_1$ dislocations and the elastic interaction between neighbor double-core dislocations. The grain boundary is at an unstable equilibrium state if the $\boldsymbol{b}_1$ dislocations lie on the same $(01\bar{1}0)$ plane as $\boldsymbol{b}_2$ and $\boldsymbol{b}_3$ dislocations. The interaction between the $\boldsymbol{b}_1$ array and $\boldsymbol{b}_2/\boldsymbol{b}_3$ array is repulsive when the distance between them is smaller than the equilibrium width, and attractive when the distance between them is larger than the equilibrium width. In the 20H/Mg and 18R/Mg incoherent interfaces, $60R_1$ and 54R, with a width of about 3.4 nm ($2.2y_0$) is observed between $\boldsymbol{b}_1$ pure edge Shockley partial dislocations array and $\boldsymbol{b}_2/\boldsymbol{b}_3$ mixed Shockley partial dislocations array [42].

5 Conclusion

In the present study, the detailed analysis of the non-equilibrium $Mg_{97}Zn_1Y_{1.6}Ca_{0.4}$ alloy was conducted through Cs-modified HAADF-STEM imaging, providing atomic-level insights into the morphology, distribution, crystal structures, and interface structures of LPSO structures. The alloy reveals a high density of ultra-fine LPSO structures. Significantly, four novel polytypes of LPSO structures are identified: 66H, 20H, 116L, and $60R_1$. The 66H LPSO structure, in particular, features a stacking sequence of $F2F3\bar{F}3F2(F6)_4$ and includes a 6-Mg component.

Acknowledgments

This work is supported by the open research fund of Songshan Lake Materials Laboratory (No. 2022SLABFN08), Guangxi Science and Technology Base and Talents Special Project (Nos. Guike AD20297034 and AD21220053), the National Natural Science Foundation of China (No. 51801214 and 52171021), the Research Start-up Funding from Guangxi University of Science and Technology (No. 03200150), the Middle-aged and Young Teachers' Basic Ability Promotion Project of Guangxi (No. 2022KY0329).

Conflict of interest

The authors declare that they have no known competing financial interests or personal relationships that could have appeared to influence the work reported in this paper.

References

[1] Prasad S S V, Prasad S B, Verma K, et al. The role and significance of magnesium in modern day research–A review. J. Magnes. Alloys, 2022, 10(1): 1–61. https://doi.org/10.1016/j.jma.2021.05.012

[2] Bairagi D, Mandal S. A comprehensive review on biocompatible Mg-based alloys as temporary orthopaedic implants: Current status, challenges, and future prospects. J. Magnes. Alloys, 2022, 10(3): 627–669. https://doi.org/10.1016/j.jma.2021.09.005

[3] Razzaghi M, Hirzadeh M, Emamy M. Unraveling the effects of Zn addition and hot extrusion process on the microstructure and mechanical properties of as-cast Mg-2Al magnesium alloy. Vacuum, 2019, 167: 214–222. https://doi.org/10.1016/j.vacuum.2019.06.013

[4] Chaudry U M, Tekumalla S, Gupta M, et al. Designing highly ductile magnesium alloys: Current status and future challenges. Crit. Rev. Solid State, 2022, 47(2): 194–281. https://doi.org/10.1080/10408436.2021.1947185

[5] Cha J W, Jin S C, Jung J G, et al. Effects of homogenization temperature on microstructure and mechanical properties of high-speed-extruded Mg-5Bi-3Al alloy. J. Magnes. Alloys, 2022, 10(10): 2833–2846. https://doi.org/10.1016/j.jma.2021.07.007

[6] Abedi H, Emamy M, Rassizadehghani J, et al. Enhanced mechanical properties of as-cast rare earth bearing magnesium alloy via elevated-temperature homogenization. Mater. Today. Commun., 2022, 31: 103821. https://doi.org/10.1016/j.mtcomm.2022.103821

[7] Shi G L, Yuan J W, Li T, et al. Enhanced precipitation strengthening of extruded Mg-8 wt.% Al-0.5 wt.% Zn (AZ80) magnesium alloy by extension twinning. Mat. Sci. Eng. A, 2020, 774: 138906. https://doi.org/10.1016/j.msea.2019.138906

[8] Alizadeh R, Wang J, LLorca J. Precipitate strengthening of pyramidal slip in Mg-Zn alloys. Mat. Sci. Eng. A, 2021, 804: 140697. https://doi.org/10.1016/j.msea.2020.140697

[9] Gerashi E, Alizadeh R, Langdon T G. Effect of crystallographic texture and twinning on the corrosion behavior of Mg alloys: A review. J. Magnes. Alloys, 2022, 10(2): 313–325. https://doi.org/10.1016/j.jma.2021.09.009

[10] Wu J, Jin L, Dong J, et al. The texture and its optimization in magnesium alloy. J. Mater. Sci. Tech., 2020, 42: 175–189. https://doi.org/10.1016/j.jmst.2019.10.010

[11] Liu P, Jiang H T, Cai Z X, et al. The effect of Y, Ce and Gd on texture, recrystallization and mechanical property of Mg-Zn alloys. J. Magnes. Alloys, 2016, 4(3): 188–196. https://doi.org/10.1016/j.jma.2016.07.001

[12] Mehranpour M S, Heydarinia A, Emamy M, et al. Enhanced mechanical properties of AZ91 magnesium alloy by inoculation and hot deformation. Mat. Sci. Eng. A, 2021, 802: 140667. https://doi.org/10.1016/j.msea.2020.140667

[13] Inoue A, Kawamura Y, Matsushita M, et al. Novel hexagonal structure and ultrahigh strength of magnesium solid solution in the Mg-Zn-Y system. J. Mater. Res., 2001, 16: 1894–1900. https://doi.org/10.1557/JMR.2001.0260

[14] Kawamura Y, Hayashi K, Inoue A, et al. Rapidly solidified powder metallurgy $Mg_{97}Zn_1Y_2$ alloys with excellent tensile yield strength above 600 MPa. Mater. Trans., 2001, 42(7): 1172–1176. https://doi.org/10.2320/matertrans.42.1172

[15] Shao X H, Yang Z Q, Ma X L. Strengthening and toughening mechanisms in Mg-Zn-Y alloy with a long period stacking ordered structure. Acta. Mater., 2010, 58(14): 4760–4771. https://doi.org/10.1016/j.actamat.2010.05.012

[16] Zhang J, Xu J, Cheng W, et al. Corrosion behavior of Mg-Zn-Y alloy with long-period stacking ordered structures. J. Mater. Sci. Tech., 2012, 28(12): 1157–1162. https://doi.org/10.1016/S1005-0302(12)60186-8

[17] Yamasaki M, Hayashi N, Izumi S, et al. Corrosion behavior of rapidly solidified Mg-Zn-rare earth element alloys in NaCl solution. Corros. Sci., 2007, 49(1): 255–262. https://doi.org/10.1016/j.corsci.2006.05.017

[18] Kawamura Y, Kasahara T, Izumi S, et al. Elevated temperature $Mg_{97}Y_2Cu_1$ alloy with long period ordered structure. Scr. Mater., 2006, 55(5): 453–456. https://doi.org/10.1016/j.scriptamat.2006.05.011

[19] Kawamura Y, Yamasaki M. Formation and mechanical properties of $Mg_{97}Zn_1RE_2$ alloys with long-period stacking ordered structure. Mater. Trans., 2007, 48(11): 2986–2992. https://doi.org/10.2320/matertrans.MER2007142

[20] Itoi T, Takahashi K, Moriyama H, et al. A high-strength Mg-Ni-Y alloy sheet with a long-period ordered phase prepared by hot-rolling. Scr. Mater., 2008, 59(10): 1155–1158. https://doi.org/10.1016/j.scriptamat.2008.08.001

[21] Matsuda M, Ii S, Kawamura Y, et al. Variation of long-period stacking order structures in rapidly solidified $Mg_{97}Zn_1Y_2$ alloy. Mater. Sci. Eng. A, 2005, 393: 269–274. https://doi.org/10.1016/j.msea.2004.10.040

[22] Abe E, Ono A, Itoi T, et al. Polytypes of long-period stacking structures synchronized with chemical order in a dilute Mg-Zn-Y alloy. Phil. Mag. Lett., 2011, 91(10): 690–696. https://doi.org/10.1080/09500839.2011.609149

[23] Shao X H, Yang H J, De Hosson J T, et al. Microstructural characterization of long-period stacking ordered phases in $Mg_{97}Zn_1Y_2$ (at.%) alloy. Microsc. Microanal., 2013, 19(6): 1575–1580. https://doi.org/10.1017/S1431927613012750

[24] Ma S Y, Liu L M, Wang S Q. The clustering of Zn_6Y_9 and its predominant role in long period stacking order phases in Mg-Zn-Y alloys: A first-principles study. Mater. Sci. Forum., 2013, 749: 569–576. https://doi.org/10.4028/www.scientific.net/MSF.749.569

[25] Saal J E, Wolverton C. Thermodynamic stability of Mg-Y-Zn long-period stacking ordered structures. Scr. Mater., 2012, 67(10): 798–801. https://doi.org/10.1016/j.scriptamat.2012.07.013

[26] Egusa D, Abe E. The structure of long period stacking/order Mg-Zn-RE phases with extended non-stoichiometry ranges. Acta. Mater., 2012, 10(1): 166–178. https://doi.org/10.1016/j.actamat.2011.09.030

[27] Zhu Y M, Morton A J, Nie J F. The 18R and 14H long-period stacking ordered structures in Mg-Y-Zn alloys. Acta. Mater., 2010, 58(8): 2936–2947. https://doi.org/10.1016/j.actamat.2010.01.022

[28] Yamasaki M, Matsushita M, Hagihara K, et al. Highly ordered 10H-type long-period stacking order phase in a Mg-Zn-Y ternary alloy. Scr. Mater., 2014, 78: 13–16. https://doi.org/10.1016/j.scriptamat.2014.01.013

[29] Kishida K, Yokobayashi H, Inui H. The most stable crystal structure and the formation processes of an order-disorder (OD) intermetallic phase in the Mg-Al-Gd ternary system. Philos. Mag., 2013, 93(21): 2826–2846. https://doi.org/10.1080/14786435.2013.790566

[30] Yokobayashi H, Kishida K, Inui H, et al. Enrichment of Gd and Al atoms in the quadruple close packed planes and their in-plane long-range ordering in the long period stacking-ordered phase in the Mg-Al-Gd system. Acta. Mater., 2011, 59(19): 7287–7299. https://doi.org/10.1016/j.actamat.2011.08.011

[31] Jin Q Q, Fang C F, Mi S B. Formation of long-period stacking ordered structures in $Mg_{88}M_5Y_7$ (M=Ti, Ni and Pb) casting alloys. J. Alloy. Compd., 2013, 568(15): 21–25. https://doi.org/10.1016/j.jallcom.2013.03.061

[32] Mi S B, Jin Q Q. New polytypes of long-period stacking ordered structures in Mg-Co-Y alloys. Scr. Mater., 2013, 68(8): 635–638. https://doi.org/10.1016/j.scriptamat.2012.12.025

[33] Jin Q Q, Shao X H, Hu X B, et al. New polytypes of LPSO structures in an Mg-Co-Y alloy. Philos. Mag., 2017, 97(1): 1–16. https://doi.org/10.1080/14786435.2016.1241909

[34] Jin Q Q, Shao X H, Peng Z Z, et al. Crystallographic account of an ultra-long period stacking ordered phase in an $Mg_{88}Co_5Y_7$ alloy. J. Alloy. Compd., 2017, 693: 1035–1038. https://doi.org/10.1016/j.jallcom.2016.09.279

[35] Luo Z P, Zhang S Q. High-resolution electron microscopy on the X-Mg12ZnY phase in a high strength Mg-Zn-Zr-Y magnesium alloy. J. Mater. Sci. Lett., 2000, 19: 813–815. https://doi.org/10.1023/A:1006793411506

[36] Saal J E, Wolverton C. Thermodynamic stability of Mg-based ternary long-period stacking ordered structures. Acta. Mater., 2014, 68: 325–338. https://doi.org/10.1016/j.actamat.2013.10.055

[37] Xu C, Nakata T, Oh-Ishi K, et al. Improving creep property of Mg-Gd-Zn alloy via trace Ca addition. Scr. Mater., 2017, 139: 34–38. https://doi.org/10.1016/j.scriptamat.2017.06.012

[38] Wan D, Wang Y, Dong S, et al. Improving corrosion resistance of high strength Mg-Zn-Y alloy through Ca addition. Corros. Eng. Sci. Technol., 2022, 57: 789–795. https://doi.org/10.1080/1478422X.2022.2127637

[39] Wang J, Zhang J S, Zong X M, et al. Effects of Ca on the formation of LPSO phase and mechanical properties of Mg-Zn-Y-Mn alloy. Mater. Sci. Eng. A, 2015, 648: 37–40. https://doi.org/10.1016/j.msea.2015.09.046

[40] Jin Q Q, Shao X H, Hu X B, et al. New polytypes of long-period stacking ordered structures in a near-equilibrium $Mg_{97}Zn_1Y_2$ alloy. Phil. Mag. Lett., 2017, 97(5): 180–187. https://doi.org/10.1080/09500839.2017.1311426

[41] Jin Q Q, Shao X H, Yang L X, et al. Stacking faults and growth twins in long-period stacking ordered structures in a near-equilibrium $Mg_{97}Zn_1Y_2$ alloy. Mater. Charact., 2020, 165: 110395. https://doi.org/10.1016/j.matchar.2020.110395

[42] Jin Q Q, Shao X H, Zheng S J, Y et al. Interfacial dislocations dominated lateral growth of long-period stacking ordered phase in Mg alloys. J. Mater. Sci. Tech., 2021, 61: 114–118. https://doi.org/10.1016/j.jmst.2020.05.045

[43] Jin Q Q, Shao X H, Li J M, et al. The role of melt cooling rate on the interface between 18R and Mg matrix in $Mg_{97}Zn_1Y_2$ alloys. J. Magnes. Alloys, 2023, 11: 2883–2890. https://doi.org/10.1016/j.jma.2021.11.010

[44] Liu C, Zhu Y M, Luo Q, et al. A 12R long-period stacking-ordered structure in a Mg-Ni-Y alloy. J. Mater. Sci. Tech., 2018, 34(12): 2235–2239. https://doi.org/10.1016/j.jmst.2018.06.015